PAPER

Check for updates

Conical shell illumination incorporating a moving aperture for depth-resolved high-energy X-ray diffraction

Daniel Spence,[a] Anthony Dicken,[a] David Downes,[a] Keith Rogers[b] and Paul Evans [ID] *[a]

In many applications, the main limitation of X-ray absorption methods is that the signals measured are a function of the attenuation coefficient, which tells us almost nothing about the chemical or crystallographic nature of objects under inspection. To calculate fundamental crystallographic parameters requires the measurement of diffracted photons from a sample. Standard laboratory diffraction methods have been refined for well over a century and provide 'gold standard' structural models for well-prepared samples and single crystals but have little applicability for thick heterogeneous samples as demanded by many screening applications. We present a new high-energy X-ray diffraction probe, which in comparison with previous depth-resolving hollow beam techniques, requires a single beam, point detector and a simple swept aperture to resolve sample signatures at unknown locations within an inspection space. We perform Monte Carlo simulations to support experiments on both single- and multiple-material localisation and identification. The new probe is configured and tested using low-cost commercial components to provide a rapid and cost-effective solution for applications including explosives detection, process control and diagnostics.

Introduction

X-ray diffraction (XRD) techniques for probing molecular structures within heterogeneous objects can be greatly beneficial to fields including explosives detection systems,[1–3] food quality and safety,[4] combinatorial screening,[5] bone quality,[6–8] and cancer diagnostics.[9] The versatility of X-rays as a non-destructive 'molecular' probe stems from their relatively short wavelength of the order of 10^{-10} m.[10] Probing photons can interact with the sample's molecular structure to produce coherently scattered (signal) photons, which can escape from the sample without energy loss. The knowledge of both the energy and trajectory of such photons enables the calculation of material characterisation information. This process is the basis of crystallography and powder diffraction.[11] However, while X-ray diffraction (XRD) offers perhaps the most specific method of material phase identification it remains restricted to the laboratory. For example, although some microbeam systems are air-cooled, most standard laboratory diffractometers usually require water cooling as thermionic X-ray generation is <1% efficient. However, the relatively low energy of the interrogating photons *e.g.*, Cu Kα radiation ~8 keV results in near-surface specimen depths of around a fraction of a mm. Thus, while the standard method has been refined for well over a century and provides 'gold standard' structural resolution for well-prepared samples and single crystals it has little applicability for thick heterogeneous samples. The evaluation of extended regions of interest along the probing direction requires at least an order of magnitude increase in photon energies for many screening applications. For example, the detection of concealed explosives in aviation luggage screening usually requires ~140 keV photons. In addition, a practical probe would require resolving explosives at unknown positions along the beam in the presence of 'cluttering' materials both of which individually would confound a standard approach.

Recent developments in XRD-based, spatially resolved materials identification techniques often require collimation into narrow pencil, or fan beams and can require either extended measurement times,[12] or powerful X-ray sources,[13] to ensure sufficient photon statistics for material identification. Rapid material identification by energy-dispersive XRD is possible at 48 mAs to 0.4 mAs but at the expense of spatial resolution.[14] In addition, tomographic XRD implementation strategies have been investigated including 3DXRD,[15] TEDDI,[16,17] XDi,[18] SICSI,[13] and XRD-CT,[19–23] and all have been individually adapted to their proposed applications.

[a]*Imaging Science Group, Rosalind Franklin Building, Clifton, Nottingham Trent University, Nottingham, UK. E-mail: paul.evans@ntu.ac.uk*
[b]*Cranfield Forensic Institute, Cranfield University, Shrivenham, Swindon, UK*

Focal construct technology (FCT) is a technique, which uses an annular beam of radiation and has been designed to improve such shortcomings.[24–26] When an annular beam is incident normally on a semi- or polycrystalline material, Debye cones with well-understood energy and angular relationships[11] are produced from each point of intersection within an annular gauge volume. These Debye cones overlap downstream in the imaging chain resulting in significantly increased scattered signal intensity.[24] FCT has been shown to deal favourably with non-ideal samples such as those exhibiting large grain size, preferred orientation (or texture),[27] and liquid samples,[28] that only exhibit short-range order. New incarnations of the FCT technique designed to work in an energy-dispersive mode (ED-FCT),[27,29] using a polychromatic X-ray beam and energy-resolving point detector exhibit advantages over angular-dispersive FCT (AD-FCT),[30–32] in terms of measurement time reduction, although with some trade-off against d-spacing resolution. In summary, prior FCT methods without collimation or modulation of the diffraction signal require the position of the sample in the beam is known to calculate structural parameters such as d-spacings. Although, AD-FCT tomography overcomes this limitation it requires raster scanning a sample through the beam and a spatially resolving detector to measure the diffracted flux.[33]

Depth-resolved ED-FCT has recently been developed by using a two-dimensional pixelated energy-resolving detector, receiving scattered flux from the sample *via* a ~2 mm pinhole between the sample and detector. The pinhole acts as a 2θ selector to provide information about the spatial origin of coherently scattered photons incident on the detector.[34] Alternatively, an energy-resolving point detector can replace the pinhole. In which case, to determine 2θ, the sample must be scanned through a dual configuration of shell beams,[35] each configured with a central detector. To recap, the former approach requires an expensive pixelated detection surface, while the latter requires 2× point detectors together with dual beam optics and a sample scanning mechanism.

Here we investigate a novel X-ray diffraction system, which combines the advantages of both the 'pinhole' and 'dual beam' ED-FCT approaches by combining a single interrogating beam and point detector *i.e.*, without the requirement for pixelated detectors or dual beams/optics and sample translation. Instead, objects under inspection are illuminated with a similar polychromatic annular X-ray beam but with a much wider circular XRD collection aperture, ~10 mm diameter optically coupled to an energy-resolving single-pixel detector. Depth information is recovered by translating the aperture along the symmetry axis of the system, providing a cumulative interrogation of a three-dimensional object, along one axis (z).

We perform Monte Carlo simulations to support experiments on both single- and multiple-material localisation and identification.[36]

The method described in this work uses commercial, off-the-shelf, low-cost components and has the potential to significantly enhance performance in areas such as security and industrial process control where cost-effective solutions are an important factor.

Experimental section

Materials

In this work we attempt to identify signature diffraction patterns of sucrose ($C_{12}H_{22}O_{11}$), calcite ($CaCO_3$) and calcium hydroxide ($Ca(OH)_2$). All materials are crystalline powders contained within sealed plastic cylindrical containers, with diameter, $2R_s = 90$ mm and depth, $t = 15$ mm.

Instrumentation

We perform experiments and simulations, which are analogous to our swept-aperture concept, see Fig. 1, by implementing discrete increments of the aperture position along the z-axis.

A polychromatic Hamamatsu point X-ray source, operating at 130 kV, 300 μA illuminates a bespoke tungsten optic, which transmits a conical shell of primary X-rays with a mean half-opening angle $\phi_{avg} = 3.92°$ and beam divergence $\Delta\phi = 0.05°$, as described in detail elsewhere.[27] At some distance downstream of the X-ray source is an Amptek XR-100T-CdTe energy-resolving detector module with a 3 mm diameter detection surface. The detector is placed at $z_d = 690$ mm at the origin of the $x - y$ plane. Energy resolution of the detector is ~850 eV with a total energy range of 1–130 keV.

Where the primary X-ray cone intersects a material with long-range order, placed between the X-ray source and detector, photons are diffracted under the satisfaction of Bragg's condition. The diffraction angle for a subset of these photons enables them to be received on the detector at z_d and are measured by photon counting.

A circular aperture of radius, $r_a = 4.5$ mm, rests initially in a position between the X-ray source and the detector, downstream of the inspection region of interest. The aperture transmits only scattered photons generated at the intersection of the primary X-ray cone from a potential conical volume element in space defined by the lines-of-sight of the extrema of the two-dimensional detector, through the aperture, see Fig. 2. As the aperture is translated along the z-axis, towards the detector, the specimen volume increases for relatively thick samples. For example, at some point a cumulative scatter
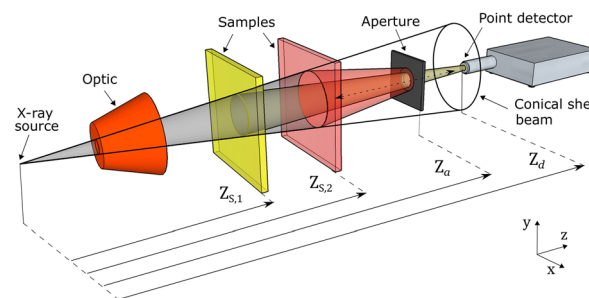

Fig. 1 Concept image of the swept aperture system with crystalline samples at z-axis positions, $z_{s,1}$ and $z_{s,2}$; circular aperture at z_a and energy-resolving detector at z_d. The aperture selects upper limits in z-space observed by the detector.

signal is received at the detector from the entire intersection volume for $z \leq z_{max}$, as determined by the aperture dimensions and relative position during the translation.

Depth information is recovered by evaluating the additional photons transmitted through the aperture (and reaching the detector) with each increment in its position, z_a relative to the previous position, $z_a - \Delta z_a$ where Δz_a is small. This is analogous to a continuously moving aperture where $\Delta z_a = z_a \Delta t$, and z_a is the translation velocity of the aperture along the z-axis. With each new aperture position, the detector observes an additional contribution to the total diffraction signal, which can be assigned to some additional specimen/intersection region in space.

Considering the two-dimensional $y - z$ plane of the system represented in Fig. 1 (at $x = 0$), there are multiple intersection points (Z_L, Z_B, Z_T, Z_R) between the cone of primary X-rays and lines-of-sight of the extrema of the detector. The detector lines-of-sight are limited by the aperture dimensions and position, illustrated in Fig. 2.

For a given aperture increment, $z_a \rightarrow z_a + \Delta z_a$ the detector receives additional diffracted photons originating within the additional intersection of the "two volumes". There exists some central position, z_C which the detector can be said to observe for a given aperture window $z_a \rightarrow z_a + \Delta z_a$. The locations of these intersection points are:

$$Z_T = \frac{r_d z_a + r_a z_d}{[r_d + r_a + (z_d - z_a)\tan(\phi_{max})]} \tag{1a}$$

$$Z_B = \frac{r_d z_a - r_a z_d}{[r_d - r_a + (z_a - z_d)\tan(\phi_{max})]} \tag{1b}$$

$$Z_R = \frac{r_d z_a + r_a z_d}{[r_d + r_a + (z_d - z_a)\tan(\phi_{min})]} \tag{1c}$$

$$Z_L = \frac{r_d z_a - r_a z_d}{[r_d + r_a + (z_a + z_d)\tan(\phi_{min})]}. \tag{1d}$$

We find that $\frac{Z_R - Z_T}{Z_R - Z_L} \ll 1$, which indicates that beam divergence is negligible in this system when considering the range of z-space observed by the detector for a given aperture

position. The central position of the observation range can be assumed to be the mid-point between Z_R and Z_L

$$z_C = \frac{1}{2}(Z_R + Z_L). \tag{2}$$

The aperture radius, r_a and the detector half-width, r_d are both fixed, as is the down-stream detector location z_d. The uncertainty in sample position is:

$$\Delta z_C = \frac{1}{2}(Z_R - Z_L). \tag{3}$$

Within the range of Z_C observable in the above geometry, the presence of materials with long-range order will generate coherent scattering (diffraction) in the form of overlapping polychromatic Debye cones,[27] impinging on the detector. If the one-dimensional spatial density (along the z-axis) of each diffracting object is described by a Gaussian profile, the total diffracted photon count observed at the detector can be modelled as a linear sum of the integrals of these Gaussian profiles; each term in the sum corresponding to an individual sample, S_n at position $z_{s,n}$. This *Linear Sum of Gaussian Integrals* (LSGI) model uses, as the integral of a Gaussian function, the *error function*. A constant term $c_{s,0}$ is included to account for system noise and miscellaneous scattering from the system upstream of the minimum interrogation volume.

$$f(z_C) = c_{s,0} + \sum_{n=1}^{N} \int_0^{z_j} A_n e^{-\left(\frac{z_C - z_{s,n}}{\sqrt{2}\sigma}\right)^2} dz_C \tag{4a}$$

$$f(z_C) = c_{s,0} + \sum_{n=1}^{N} a_n erf\left(\frac{z_C - z_{s,n}}{b}\right) \tag{4b}$$

The LSGI model's primary parameters are the set of $z_{s,n}$ indicating the presence of diffracted photons from the nth object entering the line-of-sight of the detector. To extract the contributing Gaussian profiles observed during the aperture sweep, we take the first derivative the LSGI fit.

$$f'(z_C) = \sum_{n=1}^{N} A_n e^{-\left(\frac{z_C - z_{s,n}}{\sqrt{2}\sigma}\right)^2} \tag{5}$$

The centres of the contributory Gaussians are identified by zero-crossing points in the second derivative of the LSGI fit. Having obtained estimates for the location of each diffracting material in z-space, one can calculate the appropriate $2\theta_n$ and material d-spacing values for corresponding photons arriving at the centre of the energy-resolving detector.

$$2\theta_n = \tan^{-1}\left(\frac{z_{s,n}\tan\phi_{avg}}{(z_d - z_{s,n})}\right) + \phi_{avg} \tag{6a}$$

And from Bragg's condition.

$$d_{\lambda,n} = \frac{\lambda}{2\sin\theta_n} \tag{6b}$$

Here, $2\theta_n$ is the diffraction angle; ϕ_{avg} is the average half-opening angle of the primary beam; $\lambda = \frac{hc}{E}$ is the wavelength
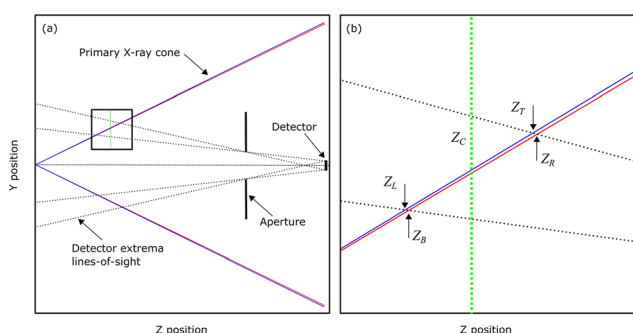

Fig. 2 Two-dimensional side-view schematic of the swept aperture system with (a) intersection of the primary X-ray cone with lines-of-sight of detector and (b) close view of intersection points (Z_L, Z_B, Z_T, Z_R) and mid-point of detector observation range for a given aperture position (z_C).

of diffracted photons observed at energy E; h is Planck's constant and c is the speed of light in a vacuum.

Monte Carlo simulations

To support the experimental work, we simulate the response of an energy-resolved X-ray detector under similar-geometry, swept-aperture conditions to those described in previous sections.

Two systems are investigated; (i) a single sample with depth, $t = 15$ mm comprised of sucrose ($C_{12}H_{22}O_{11}$), located at 220 mm from the X-ray source, and (ii) a series of two $t = 15$ mm samples, calcium hydroxide ($Ca(OH)_2$) and calcite ($CaCO_3$), the former being positioned at 160 mm from the source and the latter at 280 mm from the source.

For all simulations, the aperture is initially at $z_a = 350$ mm and increases to 680 mm in steps of $\Delta z_a = 1$ mm. Taking a 0.1 s exposure time per aperture position, the total equivalent continuous sweep duration would be ~33 s and a sweep velocity of 10 mm s^{-1}.

Annular beam experiments

An annular beam is realized with a geometry as in Fig. 1 and 2 such that $z_D = 690$ mm, $\phi_{min} = 3.87°$ and $\phi_{max} = 3.97°$.

In the first set of experiments (i) we replicate the simulation of sucrose ($C_{12}H_{22}O_{11}$) contained in cylindrical plastic containers with sample depth $t = 15$ mm. The sucrose sample is placed at ~220 ± 10 mm from the X-ray source. A second set of experiments (ii) replicates the simulation of $t = 15$ mm calcium hydroxide ($Ca(OH)_2$) and $t = 15$ mm calcite ($CaCO_3$). The powder samples are placed at ~160 ± 10 mm and ~280 ± 10 mm, respectively.

In both sets of experiments, single- and multi-sample, the aperture is initially at $z_a = 350$ mm and increases to 680 mm in steps of $\Delta z_a = 1$ mm. The photon collection time at each aperture position is either 0.1 or 0.02 seconds, producing total equivalent sweep durations of ~33 s and 6.6 s respectively, with corresponding aperture sweep velocities of 10 mm s^{-1} or 50 mm s^{-1}.

Spatial sampling

In both simulation and experiment, we sample at regular intervals in z_a, collecting photons for a period of 0.1 seconds or 0.02 seconds. This is analogous to a constant aperture sweep velocity of 10 mm s^{-1} or 50 mm s^{-1}, respectively. Additionally, there is a non-linear relationship between z_a and z_C, leading to a non-linear sampling of z-space, weighted towards low z. The equivalent continuously swept aperture would be translated at a constant velocity, $\dot{z}_a$ with acceleration $\ddot{z}_a = 0$. To sample z-space at regular intervals would require translation of the aperture with $\dot{z}_a = \dot{z}_a(z_a)$ i.e., non-zero acceleration.

The sampling rate is determined by the aperture translation interval, or the equivalent aperture sweep velocity in a continuously translated system. By increasing either, the aperture translation interval or sweep velocity we can sample z-space more sparsely and therefore reduce measurement times. The effect of this sparse sampling is discussed with reference to experiment measurements.

Results and discussion

Monte Carlo simulation

A single $t = 15$ mm region of sucrose ($C_{12}H_{22}O_{11}$) is simulated in the beam path of the annular source described above. Fig. 3 illustrates the energy-resolved intensity measurements at the detector as the aperture sweep enables an increasingly large intersection volume (and solid angle) from which diffracted photons may be detected.

The energy spectrum at each aperture position is integrated (see Fig. 3(b)), revealing a step-like function of aperture position, with a zero-value baseline (instrument noise is not simulated). The rising-edge feature is due to the increasing specimen volume interrogated as afforded by the moving aperture. The response plateau occurs when the maximum specimen thickness remains visible to the detector. A more precise assessment of the sample location requires application of the model in eqn 4(a) and 4(b) to the integrated detector intensity (Fig. 3(b)). The location of sucrose, predicted at the maximum of eqn (5), is calculated as 225 ± 38 mm from the X-ray source. The 'true' spatial range of sucrose in this simulation is 220–235 mm.

In Fig. 4 we reconstruct the diffractogram (with reference standard for comparison) of the object located at 220–235 mm by integration of the detector intensity within each energy bin collected along the plateau region of Fig. 3(b), i.e., $z_C > 350$ mm.

Next, we simulate the presence of multiple crystalline samples; calcium hydroxide ($Ca(OH)_2$) and calcite ($CaCO_3$), each with $t = 15$ mm and separated by a centre-to-centre distance of 220 mm along the z-axis. The energy-resolved and energy-integrated detector intensities are shown in Fig. 5.

The presence of two crystalline objects in the conical beam path results in a series of step changes in total photon count at the detector and plateau regions. The first plateau, τ_1 includes photons from the object closest to the source (as with the previous single sucrose example) however the second plateau, τ_2 now includes diffracted photons from both the first and second objects. To isolate the second object, we subtract
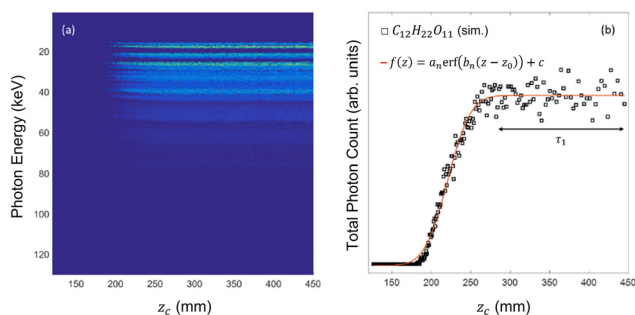

Fig. 3 Monte Carlo simulation of single $C_{12}H_{22}O_{11}$ sample at 220–235 mm with (a) energy-resolved detector intensity at each maximum observed z-axis position. The diffraction lines appear flat because once a 2θ trajectory has been 'swept through' the resultant signal is invariant to increasing z_C due to the increasing 'solid angle' of scatter capture and (b) energy-integrated detector intensity with single error function model fitted and integration period, τ_1.
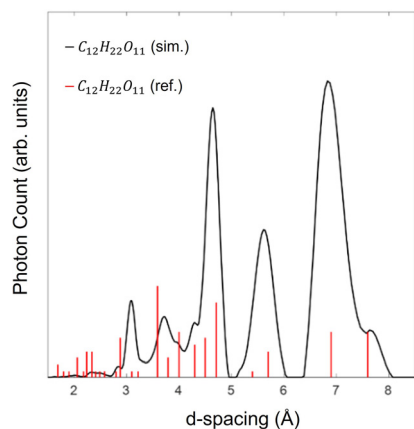
Analyst

Paper

Fig. 4 Reconstruction of simulated diffractogram of the $C_{12}H_{22}O_{11}$ sample investigated in Fig. 3. Sample location is 225–235 mm from the X-ray source with approximate corresponding diffraction angle, $2\theta = 5.8°$.

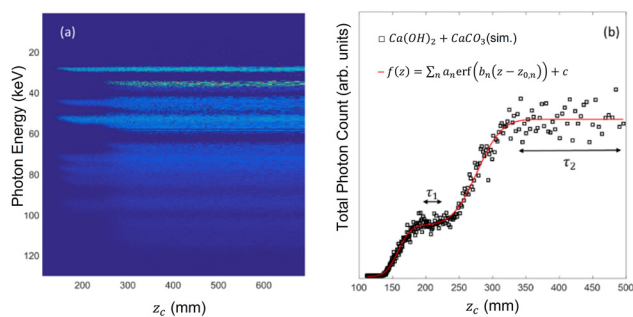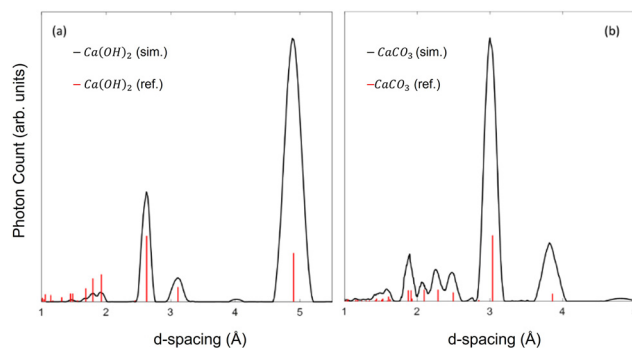**Fig. 6** Reconstruction of simulated diffractograms of the (a) $Ca(OH)_2$ and (b) $CaCO_3$ samples investigated in Fig. 5. Sample locations are (a) ~161 mm from the X-ray source with approximate corresponding diffraction angle, $2\theta = 5.1°$ and (b) ~282 mm from the X-ray source with approximate corresponding diffraction angle, $2\theta = 6.6°$.

Fig. 5 Monte Carlo simulation of multiple samples: $Ca(OH)_2$ at 160–175 mm and $CaCO_3$ at 280–295 mm with (a) energy-resolved detector intensity at each maximum observed z-axis position and (b) energy-integrated detector intensity with a sum of error functions model fitted and integration periods, τ_1 and τ_2.
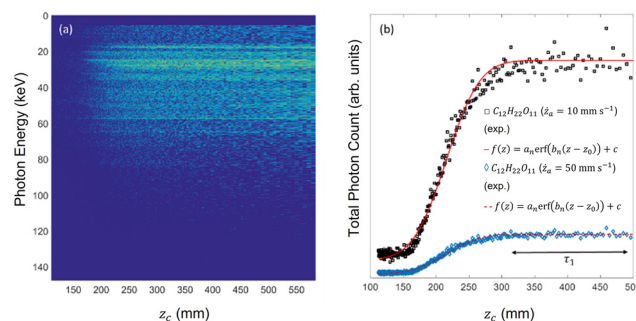
Fig. 7 Experiment measurement of a single sample at ~220 mm with (a) energy-resolved detector intensity at each maximum observed z-axis position; aperture velocity = 10 mm s^{-1} and (b) energy-integrated detector intensity with a single error function model fitted and integration period, τ_1. Measurements recorded at aperture velocities of 10 mm s^{-1} (black squares) and 50 mm s^{-1} (blue diamonds).

the integrated detector signal from the first plateau, weighted to account for sampling frequency within the respective plateaus, from the second.

The first derivative of the LSGI fit now indicates that there are two Gaussian profiles along the z-axis centred at 161 ± 26 mm and 282 ± 45 mm. The simulated locations are set at 160–175 mm and 280–295 mm, respectively. Reconstructed diffractogram and reference standards are illustrated in Fig. 6.

Swept aperture experiments

A single, $t = 15$ mm sucrose sample is illuminated by the annular source as described. Fig. 7 shows the energy-resolved and energy-integrated detector signal during the translation of the aperture. In contrast to simulation, there is now the presence of a non-zero baseline to the energy-integrated total photon count in Fig. 7(b) arising from system noise. The baseline is compensated by the constant term in the LSGI model $c_{s,0}$.

The first derivative of the LSGI model predicts a sample location $z_{s,n} = 229 ± 38$ mm or $z_{s,n} = 228 ± 38$ mm for the $\dot{z}_a =$
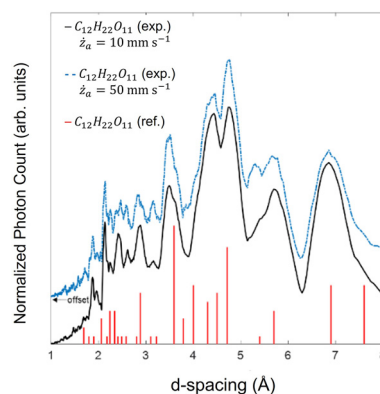
Fig. 8 Reconstruction of experiment diffractogram of the $C_{12}H_{22}O_{11}$ sample investigated in Fig. 7, with aperture velocities of 10 mm s^{-1} (black, solid) and 50 mm s^{-1} (blue, dashed). Predicted sample location is ~229 mm from the X-ray source.

Acknowledgements

References

1 S. Singh and M. Singh, *Signal Process.*, 2003, **83**(1), 31–55.
2 G. Harding and A. Harding, 8 - X-ray Diffraction Imaging for Explosives Detection, in *Counterterrorist Detection Techniques of Explosives*, ed. J. Yinon, Elsevier Netherlands, 1st edn, 2007, pp. 199–235.
3 J. A. Greenberg and J. Carpenter, 9 - X-ray diffraction for explosives detection, in *Counterterrorist Detection Techniques of Explosives*, ed. A. Kagan and J. C. Oxley, Elsevier Science, 2nd edn, 2022, pp. 315–338.
4 S. R. Purohit, L. E. Jayachandran, A. S. Raj, D. Nayak and P. S. Rao, 22 - X-ray diffraction for food quality evaluation, in *Evaluation Technologies for Food Quality*, ed. J. Zhong and X. Wang, Elsevier Woodhead, 2019, 579–594.
5 B. B. He, 11-Combinatorial Screening, in *Two-Dimensional X-Ray Diffraction*, Wiley, USA, 2009, pp. 351–368.
6 A. J. Dicken, J. P. O. Evans, K. D. Rogers, N. Stone, C. Greenwood, S. X. Godber, D. Prokopiou, J. G. Clement, D. Lyburn, R. M. Martin and P. Zioupos, *Phys. Med. Biol.*, 2015, **60**, 5803–5812.
7 C. Greenwood, K. Rogers, M. Wilson, I. Lyburn, P. Evans and D. Prokopiou, Developing focal construct technology for in vivo diagnosis of osteoporosis, *J. Phys.: Conf. Ser.*, 2019, **1151**, 012020, IOP Publishing.
8 A. J. Dicken, J. P. O. Evans, K. D. Rogers, N. Stone, C. Greenwood, S. X. Godber, J. G. Clement, I. D. Lyburn, R. M. Martin and P. Zioupos, *Sci. Rep.*, 2016, **6**, 29011.
9 A. R. Round, S. J. Wilkinson, C. J. Hall, K. D. Rogers, O. Glatter, T. Wess and I. O. Ellis, *Phys. Med. Biol.*, 2005, **50**, 4159–4168.
10 W. C. Rontgen, *Nature*, 1896, **53**(1369), 274–277.
11 W. Bragg, *Nature*, 1912, **90**, 410.
12 I. Drakos, P. Kenny, T. Fearn and R. Speller, *Crime Sci.*, 2017, **6**(1), 1.
13 J. A. Greenberg, M. Hassan, K. Krishnamurthy and D. Brady, *Analyst*, 2014, **139**, 709–713.
14 D. O'Flynn, C. Crews, I. Drakos, C. Christodoulou, M. D. Wilson, M. C. Veale and R. Speller, *J. Phys. D: Appl. Phys.*, 2016, **49**(17), 175304.
15 S. F. Nielsen, E. M. Lauridsen, D. J. Jensen and H. F. Poulsen, *J. Mater. Sci. Eng. A*, 2001, **319–321**, 179–181.
16 R. J. Cernik, K. H. Khor and C. Hansson, *J. R. Soc., Interface*, 2008, **5**(21), 477–481.
17 O. Lazzari, S. Jacques, T. Sochi and P. Barnes, *Analyst*, 2009, **134**, 1802–1807.
18 K. Wells and D. A. Bradley, *Appl. Radiat. Isot.*, 2012, **70**(8), 1729–1746.
19 A. Vamvakeros, S. D. M. Jacques, M. Di Michiel, P. Senecal, V. Middelkoop, R. J. Cernik and A. M. Beale, *J. Appl. Crystallogr.*, 2016, **49**, 485–496.
20 R. Warr, E. Ametova, R. J. Cernik, G. Fardell, S. Handschuh, J. S. Jørgensen, E. Papoutsellis, E. Pasca and P. J. Withers, *Sci. Rep.*, 2021, **11**, 20818.
21 C. K. Egan, S. D. M. Jacques, M. D. Wilson, M. C. Veale, P. Seller, A. M. Beale, R. A. D. Pattrick, P. J. Withers and R. J. Cernik, *Sci. Rep.*, 2015, **5**, 15979.
22 G. Artioli, T. Cerulli, G. Cruciani, M. C. Dalconi, G. Ferrari, M. Parisatto, A. Rack and R. Tucoulou, *Anal. Bioanal. Chem.*, 2010, **397**, 2131–2136.
23 E. Possenti, C. Conti, G. D. Gatta, N. Marinoni, M. Merlini, M. Realini, G. B. M. Vaughan and C. Colombo, *iScience*, 2022, **25**(10), 105112.
24 P. Evans, K. Rogers, J. Chan, J. Rogers and A. Dicken, *Appl. Phys. Lett.*, 2010, **97**, 204101.
25 K. Rogers, P. Evans, J. Rogers, J. Chan and A. Dicken, *J. Appl. Crystallogr.*, 2010, **43**(2), 264–268.
26 K. Rogers and P. Evans, X-ray diffraction and focal construct technology, in *X-Ray Diffraction Imaging: Technology and Applications*, ed. J. Greenberg, Taylor and Francis Group, 2019, 165–188.
27 A. Dicken, J. P. O. Evans, K. D. Rogers, C. Greenwood, S. X. Godber, D. Prokopiou, N. Stone, J. G. Clement, I. Lyburn, R. M. Martin and P. Zioupos, *Opt. Express*, 2015, **23**(10), 13443–13454.
28 D. Prokopiou, K. Rogers, P. Evans, S. Godber and A. Dicken, *Appl. Radiat. Isot.*, 2013, **77**, 160–165.
29 F. Li, Z. Liu, T. Sun, B. Jiang and Y. Zhu, *J. Chem. Phys.*, 2016, **144**, 104201.
30 X. H. Chen, B. Li, T. Xue and J. Li, *Rev. Sci. Instrum.*, 2020, **91**, 083908.
31 D. Prokopiou, J. McGovern, G. Davies, S. Godber, P. Evans, A. Dicken and K. Rogers, *J. Appl. Crystallogr.*, 2020, **53**(4), 1073–1079.
32 A. Dicken, A. Shevchuk, K. Rogers, S. Godber and P. Evans, *Opt. Express*, 2015, **23**(5), 6304–6312.
33 P. Evans, K. Rogers, A. Dicken, S. Godber and D. Prokopiou, *Opt. Express*, 2014, **22**(10), 11930–11944.
34 A. Dicken, J. P. O. Evans, K. D. Rogers, D. Prokopiou, S. X. Godber and M. Wilson, *Opt. Express*, 2017, **25**(18), 21321–21328.
35 A. Dicken, D. Spence, K. Rogers, D. Prokopiou and P. Evans, *Analyst*, 2018, **143**(20), 4849–4853.
36 E. B. Knudsen, A. Prodi, J. Baltser, M. Thomsen, P. K. Willendrup, M. Sanchez del Rio, C. Ferrero, E. Farhi, K. Haldrup, A. Vickery, R. Feidenhans'l, K. Mortensen, M. M. Nielsen, H. F. Poulsen, S. Schmidt and K. Lefmann, *J. Appl. Crystallogr.*, 2013, **46**(3), 679–696.
37 R. F. Karlak and D. S. Burnett, *Anal. Chem.*, 1966, **38**(12), 1741–1745.
38 L. B. McCusker, R. B. Von Dreele, D. E. Cox, D. Louër and P. Scardi, *J. Appl. Crystallogr.*, 1999, **32**(1), 36–50.